



Article

Manganese Oxide Minerals from the Xiangtan Manganese Deposit in South China and Their Application in Formaldehyde Removal

Liquan Zhao ^{1,2} , Sida Niu ^{1,2,*} , Xianglong Niu ^{1,2}, Tong Chen ^{1,2}, Yingchao Wang ^{1,2}, Lei Li ³, Fei Huang ⁴, Huaying Wu ^{1,2}, Lingchao Mo ^{1,2} and Min Zhang ^{1,2}

¹ Institute of Mineral Resources Research, China Metallurgical Geology Bureau, Beijing 101300, China; zhaoliquan@cmgb.cn (L.Z.); niuxianglong@cmgb.cn (X.N.); chentong@cmgb.cn (T.C.); wangyingchao@cmgb.cn (Y.W.); wuhuaying@cmgb.cn (H.W.); molingchao@cmgb.cn (L.M.); zhangmin@cmgb.cn (M.Z.)

² Mineral Comprehensive Utilization Research and Development Center, China Metallurgical Geology Bureau, Beijing 101300, China

³ BGRIMM Technology Group, Beijing 102628, China; lilei@bgrimm.com

⁴ Hunan Geological Exploration Institute of China Metallurgical Geology Bureau, Changsha 410001, China; hndzkcy888@163.com

* Correspondence: niusida@cmgb.cn

Abstract: Because of the nano-scale tunnel constructed by the active Mn-O octahedron in cryptomelane, cryptomelane-type manganese oxides have high activity in the oxidation of several volatile organic compounds (VOCs). Natural cryptomelane, in the form of supergene oxide manganese ore, carpets much of South China. In the lower part of the Datangpo Formation of Nanhua System on the southeastern Yangtze Platform, cryptomelane is one of the major manganese oxides in black shale of the Xiangtan manganese deposit in this deposit. Formaldehyde is a dominant indoor pollutant among volatile organic compounds (VOCs), and applications of synthetic cryptomelane have been reported to eliminate it. To study the removal capacity of naturally outcropping cryptomelane, representative samples of manganese oxide (the primary mineral component of cryptomelane) from the Xiangtan Mn deposit were analyzed in this study. The chemical composition, crystal structure and micromorphology of the manganese oxide minerals were explored using ICP-AES, XRD, EPMA, SEM and HR-TEM techniques. Fine-grained and poorly crystalline, these minerals consist primarily of cryptomelane, along with minor amounts of pyrolusite, hollandite, lithiophorite, limonite and quartz. Natural cryptomelane is a monoclinic crystal, and its cell parameters are refined. The results of catalytic tests revealed that natural cryptomelane has obvious catalytic activity in the oxidation of formaldehyde in a static environment under room temperature. This study may provide a natural mineral material as an inexpensive and efficient catalyst for the purification of formaldehyde in industrial or indoor air treatment.

Keywords: natural cryptomelane; manganese oxide minerals; catalytic oxidation; formaldehyde; Xiangtan manganese deposit; 2 × 2 tunnel structure



Citation: Zhao, L.; Niu, S.; Niu, X.; Chen, T.; Wang, Y.; Li, L.; Huang, F.; Wu, H.; Mo, L.; Zhang, M. Manganese Oxide Minerals from the Xiangtan Manganese Deposit in South China and Their Application in Formaldehyde Removal. *Minerals* **2022**, *12*, 552. <https://doi.org/10.3390/min12050552>

Academic Editors: Jean-François Blais, Donggao Zhao, Shui-Yuan Yang and Zhenyu Chen

Received: 16 February 2022

Accepted: 24 April 2022

Published: 28 April 2022

Publisher's Note: MDPI stays neutral with regard to jurisdictional claims in published maps and institutional affiliations.



Copyright: © 2022 by the authors. Licensee MDPI, Basel, Switzerland. This article is an open access article distributed under the terms and conditions of the Creative Commons Attribution (CC BY) license (<https://creativecommons.org/licenses/by/4.0/>).

1. Introduction

Manganese is a relatively active metal, and its valence states can be 0, 2+, 3+, 4+, 6+ or 7+. It has more valence states than any other elements. Thus, there are a large number of manganese minerals, including more than 30 known manganese oxides/hydroxides [1,2]. Manganese oxide materials are formed by the MnO₆ octahedra connected by various crystallographic forms (e.g., α-, β-, γ-, δ-, and ε-type MnO₂), which serve as microporous transition-metal oxides with remarkable potential in many situations [2]. They have been used as for decades as essential materials in catalysts, molecular sieves, batteries, water purifiers and numerous other industrial applications [3–5].

In recent years, catalytic oxidation has been considered to be one of the most promising means to convert formaldehyde (chemical formula CH_2O or HCHO) into CO_2 and H_2O [6–8]. Mn-based transition metal oxides show high redox properties and are quite inexpensive compared with noble-metal catalyst. Therefore, a great deal of attention has been paid to the use of synthetic of Mn-based catalysts for removing formaldehyde at room or low temperatures [9–11]. However, the application of natural manganese oxide has rarely been reported.

Complex natural manganese oxides, highly reactive mineral materials, have played an important role in the Earth's critical zone, functioning with abundant nanophases in nature [12–14]. Their structures and catalytic applications have attracted much attention because of its cost-effectiveness, plentiful reserves, and superior thermal stability. Among the varieties of manganese oxide minerals, research on the 2×2 tunnel structure cryptomelane (the Ba-bearing variety is hollandite) and the layered structure birnessite have been carried out in particular [15–17]. In nature, manganese oxide ore is difficult to identify because it contains many mineral species, and because prolonged weathering erodes its cryptocrystalline [18]. China has 54 million tons of proven manganese ore (metal) reserves, accounting for 6.65% of the global total [19]. Among the various oxides in the supergene manganese ore in south China, cryptomelane is abundant. The Xiangtan manganese deposit was developed early, and the composition, morphology and crystal structure of its cryptomelane in the secondary oxidation zone has been studied [20,21]. To investigate the performance of absorption and catalysis of formaldehyde by natural manganese oxide minerals, an integrated study was undertaken. The major manganese oxides in the Xiangtan deposit were characterized by X-ray diffraction (XRD), electron probe micro analysis (EPMA), scanning electron microscopy (SEM), transmission electron microscopy (TEM). In addition, its mineralogical features were evaluated for formaldehyde removal at room temperature.

A Total Volatile Organic Compounds (TVOC) is a health-threatening air pollutant known as “The invisible killer”. Its toxicity, irritation, carcinogenicity and special odor can cause acute damage. Formaldehyde, with its extensive sources, high toxicity and off-gassing, is the primary indoor pollutant and has been identified as carcinogenic to humans (Group 1) by the World Health Organization (WHO) [12,22]. The duration of indoor formaldehyde pollution can be 3–15 years, and it cannot be effectively eliminated by most removal methods. This study may present a natural mineral as an inexpensive and efficient catalyst for the removal of formaldehyde from industrial and indoor environments.

2. Geological Setting

The Neoproterozoic Datangpo is the most important period of manganese metallogenesis in China. The ore reserves formed are the largest, and typical deposits include the Datangpo, Daotuo, Xiushan and Xiangtan deposits in the black shale series in the lower part of the Datangpo Formation [23,24].

The Xiangtan deposit is located on the southeast margin of the Yangtze Block (Figure 1a), which is the concentrated distribution area of manganese ore. A series of deposits has been found in the area: Xiangtan, Jiutanchong, Xiangxiang, Jinshi and Nanmuchong. The strata in the study area mainly include the Neoproterozoic Banxi Group, Nanhua System Fulu Formation, Datangpo Formation, Nantuo Formation and Sinian Doushantuo Formation, listed from old to new (Figure 1b). As for the structure, the Heling anticline controls the distribution of the ore bodies. The faults in the area, as well as the concealed small folds and faults, affect the ore body.

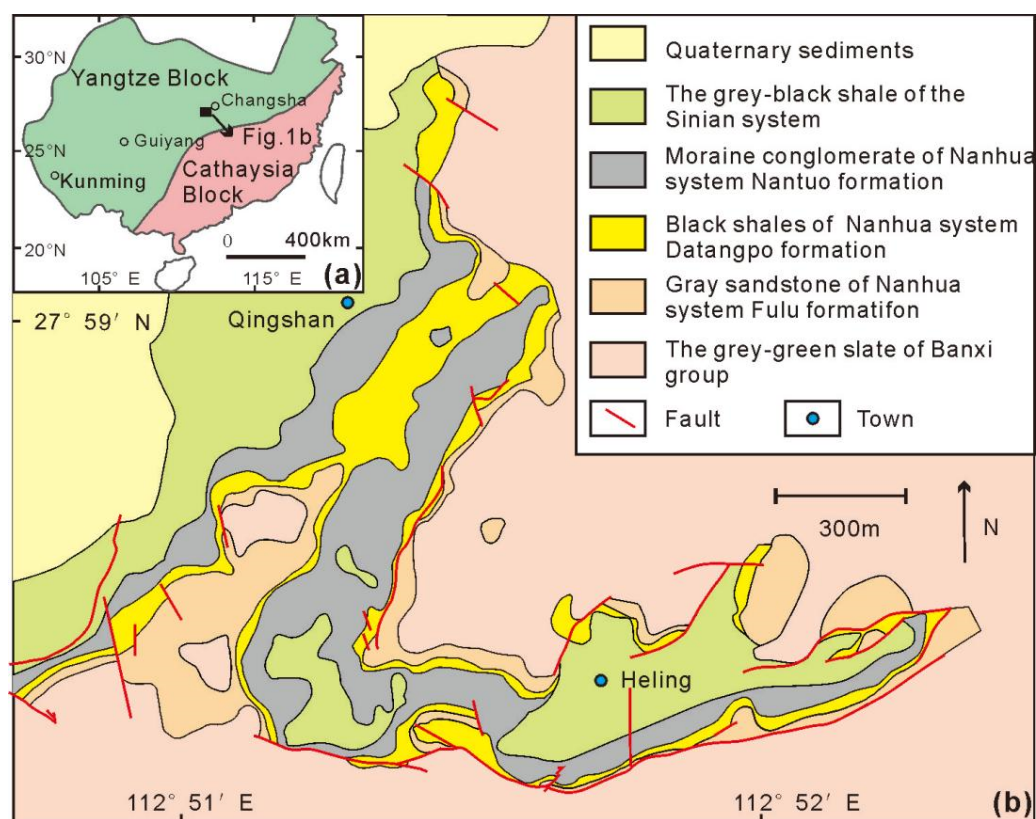


Figure 1. Tectonic sketch map of South China and the location of the study area (a) and geological sketch map of the Xiangtan manganese deposit (b).

The ore-bearing rocks are the black shale series in the lower part of the Datangpo Formation, which are generally single-layered in the host rock with the average thicknesses of 1.4 m. The total length along the strike is 7000 m, and the width along the dip is generally 250–500 m. Manganese carbonate dominates the primary manganese ore in the Xiangtan deposit, which is mainly composed of rhodochrosite or calamine along with minor amounts of manganese calcite and manganese-containing calcite. The manganese carbonate ore is mainly banded, layered and massive structure. Supergene oxide manganese ore is carpeted widely on surface, which was mainly formed by the secondary oxidation of shallow manganese carbonate ore above the diving surface. The depth of manganese oxide ore is generally 10–35 m, and the deepest is up to 50 m. It is mainly banded, oolitic, massive and colloidal.

3. Sampling and Methods

3.1. Sample Preparation

Samples were taken from the Heling mining district in the Xiangtan deposit. In contrast to the dark gray, dense, hard manganese carbonate ore, the supergene altered equivalents are friable and porous (Figure 2b,f), with a distinct black to steel-gray/slightly brownish red color and, a semi-metallic to earthy luster. In general, the hand specimens of supergene manganese oxide ore are cryptocrystalline aggregates with noticeable reniform (Figure 2a), botryoidal (Figure 2d), oolitic (Figure 2c), massive (Figure 2e), lattice-earthy (Figure 2f), and massive-vein textures (Figure 2g). The cryptomelane exhibits a metallic silvery-black luster which alternates between brownish red limonite (Figure 2b,e) and milky quartz (Figure 2g). Mn oxide ore samples were crushed, ground and screened for detailed mineralogical investigation and formaldehyde removal evaluation. Polished sections were prepared and studied for detailed mineral microscopy analysis and identification of oxide minerals. The massive raw Mn oxide ore (XTO-1) from the Xiangtan deposit was cleaned and crushed by a jaw crusher to obtain 60–200 mesh mineral powder (XTO-2) with an average MnO content

of about 48 wt.% (Table 1). When the XTO-2 was shaken in a water-filled pan, the heavier Mn oxide mineral particles sank to the bottom while the lighter ones were washed away and the MnO content of samples by manual gravity concentration (XTO-3) was increased to 63 wt.% (Table 1). Then, the Mn-oxide minerals (XTO-4) were obtained from powder after gravity concentration under a binocular microscope by hand selection. Samples were also ground in agate mortar and separated for X-ray powder diffraction (XRD), scanning electron microscopy (SEM), and transmission electron microscope (TEM).

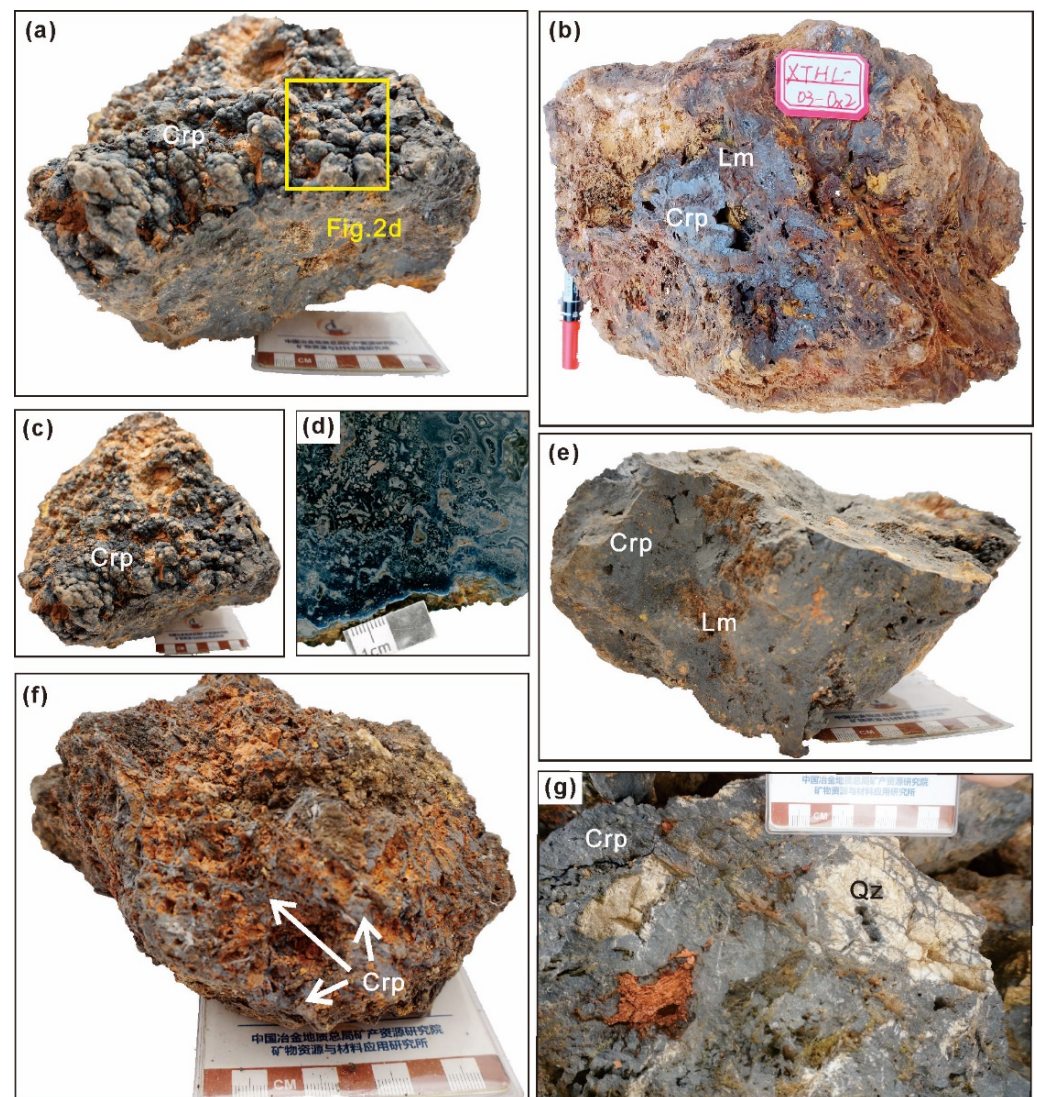


Figure 2. Representative hand specimens of the Mn-oxide ore in the Xiangtan deposit. (a) Reniform texture. (b) Massive-cellular texture; (c) oolitic and pisolitic texture; (d) botryoidal and conchoidal texture, the polished surface of location shown in (a) correspondingly; (e) massive texture; (f) lattice-earthy texture; (g) massive-vein texture; Qz—quartz; Crp—cryptomelane; Lim—limonite.

Table 1. The contents of oxides (wt.%) and LOI (Loss on ignition) of powder samples from the Xiangtan deposit.

	SiO ₂	Al ₂ O ₃	CaO	Fe ₂ O ₃	K ₂ O	MgO	MnO	Na ₂ O	P ₂ O ₅	TiO ₂	LOI
Sample XTO-2	22.94	2.81	0.16	9.44	2.43	0.073	48.11	0.14	0.84	0.037	11.39
Sample XTO-3	9.82	2.05	0.19	6.17	3.15	0.083	63.67	0.16	0.75	0.014	12.52

3.2. Mineralogical Analysis

Samples XTO-2 and XTO-3 were grounded in agate mortar and separated (<200 mesh) for Inductively Coupled Plasma Atomic Emission Spectrometry (ICP-AES). The oxides (Si, Al, Ca, Fe, K, Mg, Mn, Na, P and Ti) were detected. For the manganese content in the ore, refer to GB/T 1506-2016. The determination of other elements refers to GB/T 14506.3-2010 and ISBN 978-7-116-07130-8, and the LOI determination refers to DZG 20-01-1991. The detection limits are of SiO₂, Al, Ca, Fe, K, Mg, Mn, Na, P, and Ti, with 1000 µg/g, 500 µg/g, 500 µg/g, 500 µg/g, 500 µg/g, 500 µg/g, 20 µg/g, 1000 µg/g, 20 µg/g, 100 µg/g and 100 µg/g, respectively. The ICP-AES analyses were performed at the Environmental Science and Technology Co., Ltd. Testing Center of No.1 Bureau, CMGB.

XRD studies were performed on samples XTO-2, XTO-3 and XTO-4 (<200 mesh) using Cu K α radiation and a SmartLab 9000W X-ray powder diffractometer (Rigaku Corporation, Rigaku, Tokyo, Japan). X-ray diffraction patterns were collected between 5 and 80° (2 θ) at a scanning rate of 0.02° (2 θ) s⁻¹ (λ = 0.154 nm, 40 kV, 200 mA). For XRD indexing, the Le Bail routine (Peakfit) and manually picked peaks were combined. The Rietveld method with extraction of the structure factors (Fobs) was then used to refine the unit cell parameters. The XRD analyses were performed at the China University of Geosciences, Beijing.

XTO-3 (<200 mesh) were carbon coated and pasted onto conductive adhesive for SEM and energy dispersive spectroscopy (EDS) analysis. SEM observations were carried out on a Hitachi S-3500N scanning electron microscope (Hitachi, Tokyo, Japan) operated at 24.96 kV. EDS analysis was carried out using an INCA-300 Oxford Instrument (the UK Oxford instruments, Abingdon, UK). The SEM analyses were performed at the BGRIMM Technology Group.

TEM and high-resolution transmission electron microscopy (HRTEM). TEM images were obtained using a JEOL JEM2100 (JEOL, Tokyo, Japan) high-resolution transmission electron microscope at an accelerating voltage of 200 kV. TEM samples were prepared by depositing several droplets of a nanoparticle/ethanol mixture onto a carbon coated Cu-grid, and then treated with ion thinning. The EDS spectrum was obtained by the Oxford INCA system mounted on a TEM, which has a 10 mm² detector with 140 eV resolution. The TEM and HRTEM analyses were carried out at the BGRIMM Technology Group.

Major and minor element chemical analysis by EPMA and EDS Mapping of the Mn oxides were conducted at the Chinese Academy of Geological Sciences using a JXA-iHP200F Hyper Probe electron microprobe (JEOL, Tokyo, Japan) with a JED-2300 Analysis Station installed on it. At a 15 kV accelerating voltage, a beam current of 20 nA, a counting time of 10 s (peak position), and a beam diameter of 5 µm. Standard substances refer to GB/T 15074-2008 general rules for EPMA analysis. The relevant information of the methodology for studying the composition of manganese minerals by EPMA analysis as in Table 2. The confidence interval for estimating the value of detection limits is 1 σ .

Table 2. The methodology for studying the composition of manganese minerals by EPMA.

Element	Standard	X-ray	Crystal	Method	S. D. (%)	D. L. (ppm)
Al	02-rAl ₂ SiO ₅ -0315	Ka	TAP	ZAF	0.16	100
Si	03-SiO ₂ -0224	Ka	TAP	ZAF	0.13	120
Ca	02-CaSiO ₃ -0224	Ka	PETL	ZAF	0.14	80
Ba	21-BaSO ₄ -0312	La	PETL	ZAF	0.17	210
Mn	14-MnTiO ₃ -0224	Ka	LIF	ZAF	0.61	205
Fe	20-Fe ₃ O ₄ -0312	Ka	LIF	ZAF	0.33	320
Mg	1-MgSiO ₄ -0312	Ka	TAPH	ZAF	0.17	160
K	17-KNbO ₃ -0224	Ka	PETH	ZAF	0.21	70
Cu	23-Cu ₂ O-0312	Ka	LIF	ZAF	0.29	440
P	7-CaPO ₄ -0312	Ka	PETL	ZAF	0.34	220

3.3. Formaldehyde Removal Test

The formaldehyde removal tests were carried out at room temperature in 12.5-L airtight glass containers. Sample was dispersed on the bottom of a glass Petri dish with a diameter of 100 mm. At room temperature of 21 °C, formaldehyde solution (0.2 mL 10% formalin solution diluted in 10 mL water) was placed in 5 airtight glass containers. To compare the performance on formaldehyde removal with the natural manganese oxide mineral aggregates, the experimental conditions were container A with no sample inside; container B with XTO-3 (35 g, 200 mesh); container C with XTO-1 (volume approximately 60 cm³); container D using XTO-2 (35 g, 200 mesh); and container E with commercial product for formaldehyde decomposition (high purity synthetic birnessite with almost no impurities, half the weight of container B as 16 g). As the commercial product is pure synthetic birnessite, the same weight of 16g samples were used. Thus, weight of functional phases are coincide in natural Mn oxides sample in container B and synthetic birnessite sample in container E (16 g).

The concentrations of gaseous formaldehyde and CO₂ were monitored by an electrochemistry field gas monitor (HIKE Air-Tech Instruments, Model B6. (Hike Smart Technology Development Co., Ltd., Beijing, China) equipped with Dart Sensors J2 detector. During the catalytic oxidation reaction, formaldehyde concentration decreased and CO₂ concentration increased steadily with time. The cumulative value of CO₂ produced by the catalytic oxidation of formaldehyde was the maximum difference between the concentration of CO₂ in the container at the beginning and at the end of the reaction. The formaldehyde removal efficiency (η) was used to evaluate the performance of the sample, and was calculated according to the following equation:

$$\eta = \frac{[\text{HCHO}]_i - [\text{HCHO}]_f}{[\text{HCHO}]_i} \times 100\% \quad (1)$$

where [HCHO]_i (mg/m³) is the concentration of formaldehyde in the container with test samples (B to E), and [HCHO]_f (mg/m³) is the concentration of formaldehyde in the blank container A.

4. Results

4.1. Optical Microscopy

The Mn oxide minerals in the ore are exceptionally fine-grained and poorly crystalline (Figure 3a,d,g). Mn oxide ore consists primarily of cryptomelane (about 45%), accompanied by minor pyrolusite (about 6%), hollandite (about 8%), lithiophorite (about 7%). Along with other minerals include limonite, quartz and clays. Manganese oxide phases mainly occur when the structures of the core-rim (Figure 3c), parallel bands (Figure 3b,h) and Mn oxide matrix overprint detrital grains (Figure 3i). The limonite occurs as thin microscopic layers around the Mn oxide phases (Figure 3e). Cryptomelane and hollandite show a light, whitish green-to-off-white reflection color although sometimes the hollandite has a darker color (Figure 3b,c). Pyrolusite appears white with creamy yellow tint under reflected light, and lithiophorite is dark brownish-gray. The sample appears to contain different generations of manganese oxide precipitation: early cryptomelane precipitated to form smaller cores or bands (Figure 3b,h,i), which are surrounded by late pyrolusite, hollandite and limonite with a parallel banded structure (Figure 3b,e,h,i). The most recently formed cryptomelane always occurs in the outermost layer with fibrous and radial structures (Figure 3b,f).

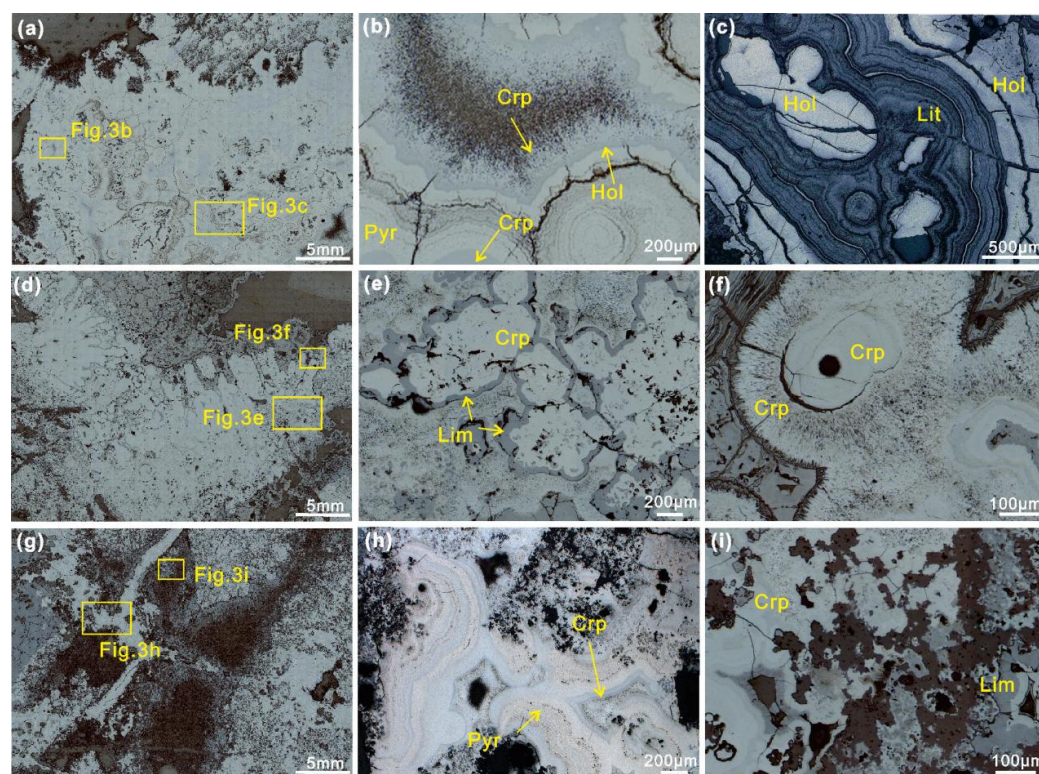


Figure 3. Reflected light micrographs of the mineralogy and textures of the Mn-oxide ore in the Xiangtan deposit. (a,d,g) Cryptocrystalline Mn oxide with colloidal structure.; (b) Cryptomelane showing light whitish green to off-white reflection color, fibrous and radial texture; (c) Hollandite and lithiophorite, annule texture; (e,i) The thin, limonite microscopic layers around the cryptomelane; (f) Cryptomelane with different mineralization stages; (h) Pyrolusite showing creamy yellow tint reflection color and a parallel banded structure. Crp—cryptomelane; Hol—hollandite; Pyr—pyrolusite; Lit—lithiophorite; Lim—limonite.

4.2. EPMA Analysis

Table S1 lists the complete data of the EPMA analysis of the manganese oxide minerals in the Xiangtan deposit, with 96 points in total. We used MnO_2 to calculate the mineral elements according to the major manganese oxide phase (essentially tetravalent oxides) in the samples. The cryptomelane is composed of MnO_2 (84.54–99.50 wt.%), K_2O (1.25–5.18 wt.%), BaO (0–2.66 wt.%), Al_2O_3 (0.17–5.76 wt.%), FeO (0.02–6.06 wt.%), CaO (0.02–0.20 wt.%), and other oxides include SiO_2 (<0.35 wt.%), P_2O_5 (<0.66 wt.%), CuO (<0.10 wt.%), MgO (<0.04 wt.%). The corresponding chemical formulas of the natural cryptomelane are $(\text{K}_{0.36\sim1.48}\text{Ba}_{0\sim1.02}\text{Ca}_{0.01\sim0.05})_{0.44\sim1.79}(\text{Mn}_{6.24\sim7.72}\text{Al}_{0\sim1.45}\text{Fe}_{0\sim1.17}\text{P}_{0\sim0.12}\text{Si}_{0.01\sim0.08})_{7.68\sim8.41}\text{O}_{16}$.

The pyrolusite is composed of MnO_2 (98.03–101.55 wt.%), K_2O (0.14–0.70 wt.%), BaO (0–0.05 wt.%), Al_2O_3 (0.12–0.92 wt.%), FeO (0.07–0.76 wt.%). The hollandite is composed of MnO_2 (59.34–93.10 wt.%), BaO (2.21–11.49 wt.%), Al_2O_3 (0.72–18.98 wt.%), K_2O (0.04–3.14 wt.%) and FeO (0–16.92 wt.%). The lithiophorite are composed of MnO_2 (58.87–64.35 wt.%), Al_2O_3 (17.67–23.82 wt.%), BaO (0–3.24 wt.%), K_2O (0–0.05 wt.%) and FeO (0.02–0.13 wt.%).

4.3. EDS Mappings

EDS mappings analysis reveals that the formation of manganese oxide minerals is complex and multistaged (Figure 4). Figure 4a shows the distribution of Fe, Mn, K and P in the samples. The parallel and concentric bands of Fe-Mn oxides and cryptomelane (Figure 4c) formed in the early stage were covered and reformed by the pure capillary and colloidal cryptomelane (Figure 4b) in the late stage.

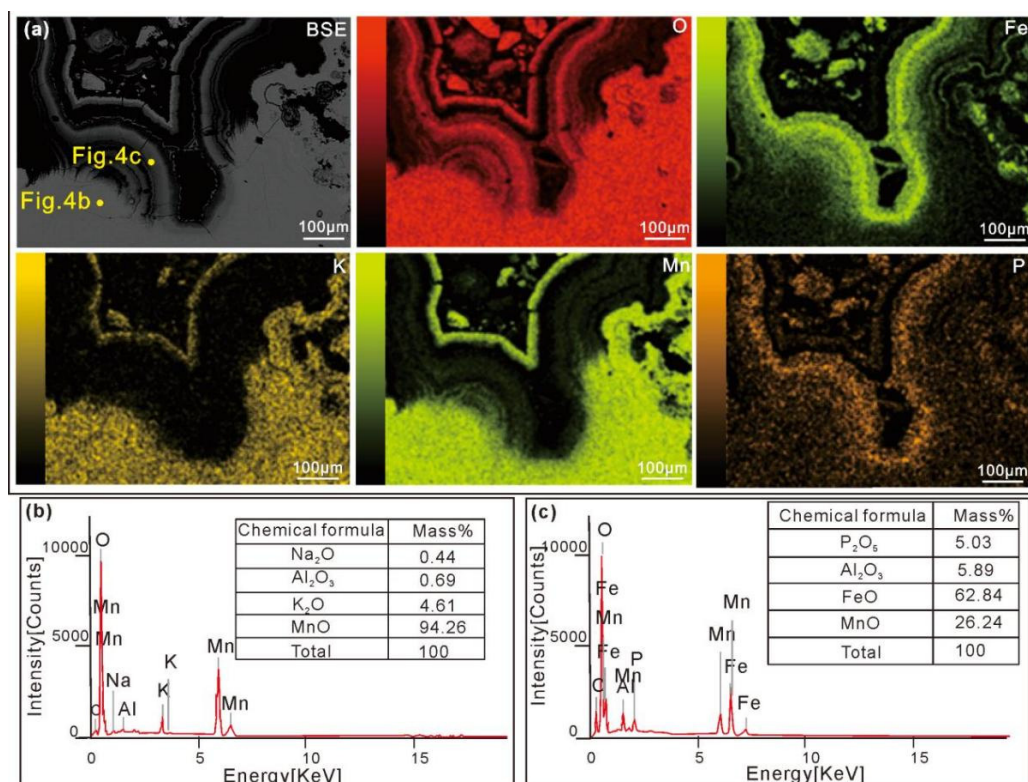


Figure 4. EDS Mapping of Mn oxide minerals in the Xiangtan deposit. (a) BSE image reveals the complexity of the microstructure and EDS Mapping showing the elemental distribution of O, Fe, K, Mn and P; (b,c) are the EDS results (analyzed points shown in (a) correspondingly).

4.4. SEM and TEM Analysis

Figure 5 shows the SEM and TEM images of cryptomelane, which takes the shape of one-dimensional nanorods. The cryptomelane crystal is acerosic and fibrous and always penetrates other crystals to form an irregular lattice or grow radially (Figure 5a). The nanocrystalline cryptomelane aggregates are usually tabular and flaky (Figure 5b,c,e) with widths less than 100 nm. The EDS result of cryptomelane is shown in Figure 5d,f. By calculating and indexing the electronic diffraction analysis through TEM (Figure 5g), the corresponding crystal plane spacings and indexes are: $d_1 = 0.2400$ nm, $d_2 = 0.2427$ nm and $d_3 = 0.6892$ nm, which are in good agreement with the lattice spacings of the (211), (004) and (101) planes of cryptomelane. The plane spacings were calculated by lattice fringes under HRTEM observation (Figure 5h). Two groups of crystal plane spacings are: $d_4 = 0.7007$ nm and $d_5 = 0.2485$ nm, and the corresponding crystal planes are (10-1) and (400) of cryptomelane. The lattice fringe in the upper left is slightly bent (Figure 5h), indicating possible lattice distortion. The fringe on the lower left is not clear, probably because of low crystallinity. When an electron beam stays on the surface of cryptomelane for a long time under TEM, its one-dimensional nanorod shape changes to pellet shape, suggesting that the cryptomelane may have strong activity (Figure 5i).

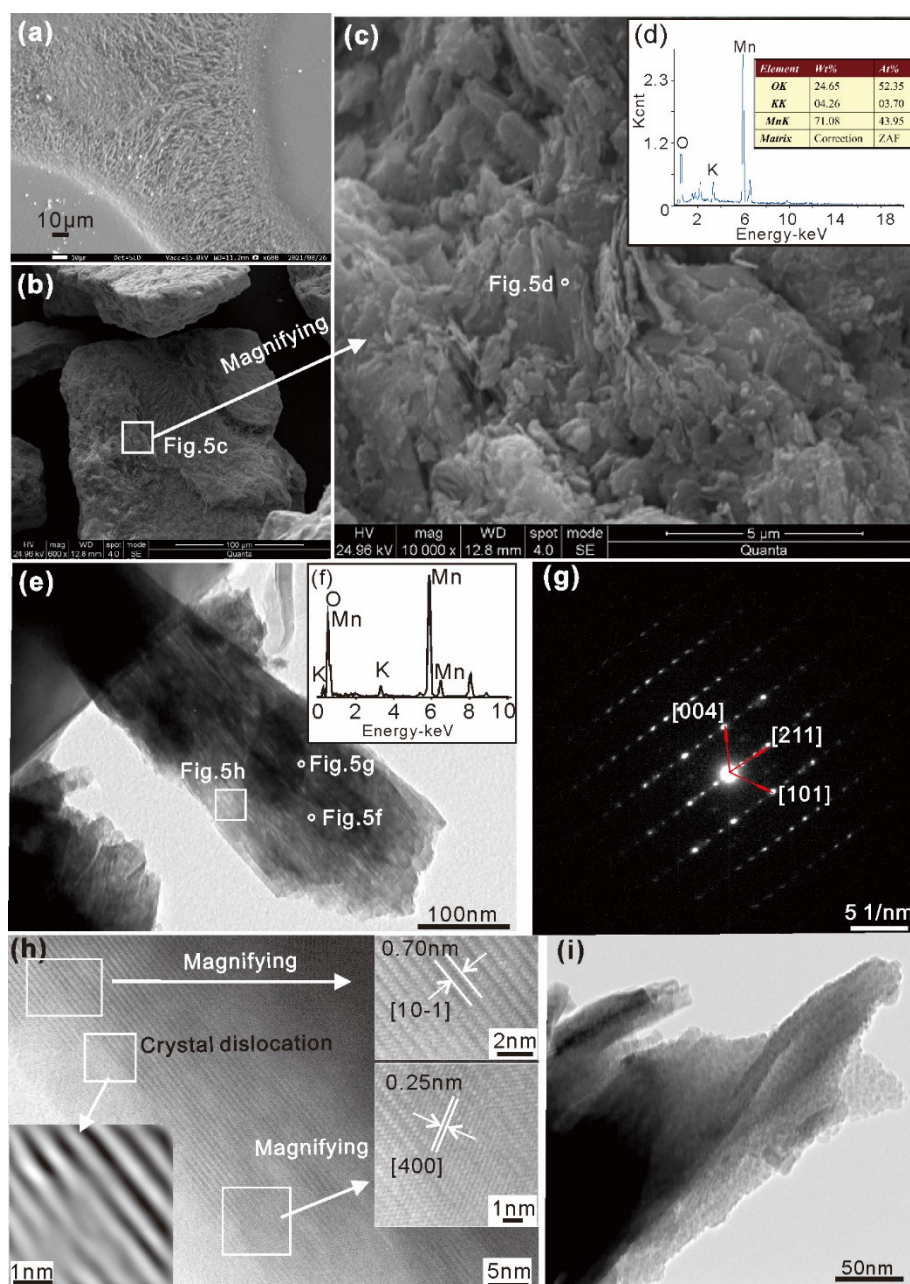


Figure 5. SEM, TEM and HRTEM images of Mn oxide ore in the Xiangtan deposit. (a–c): SEM images of cryptomelane crystal and its aggregate, with needle-like and fibrous structure. (d) The EDS results of the location shown in (c) correspondingly. (e,i): TEM images of cryptomelane aggregate. (f) The EDS results of the location shown in (e) correspondingly. (g) SAED patterns of natural cryptomelane in HRAEM. (h) Crystal lattice images of cryptomelane in HRTEM. (i) Pellet-shaped cryptomelane after a long irradiation by the electron beam.

4.5. XRD Analysis

The three greatest-intensity peaks for XTO-2, positioned at 2θ angles of 26.719° , 20.930° , and 50.216° , are due to quartz (Figure 6), which is the main gangue mineral phases with well crystallization. The three greatest-intensity peaks for samples of XTO-3 and XTO-4 are: $2\theta = 37.512^\circ$, $2\theta = 26.636^\circ$, $2\theta = 12.710^\circ$. The fourth highest-intensity peak is positioned at a 2θ of 28.627° . Their main mineral phases comprise cryptomelane, hollandite and quartz. Due to low amount and low degree of crystallinity, the presence of pyrolusite and lithiophorite were only confirmed by EPMA.

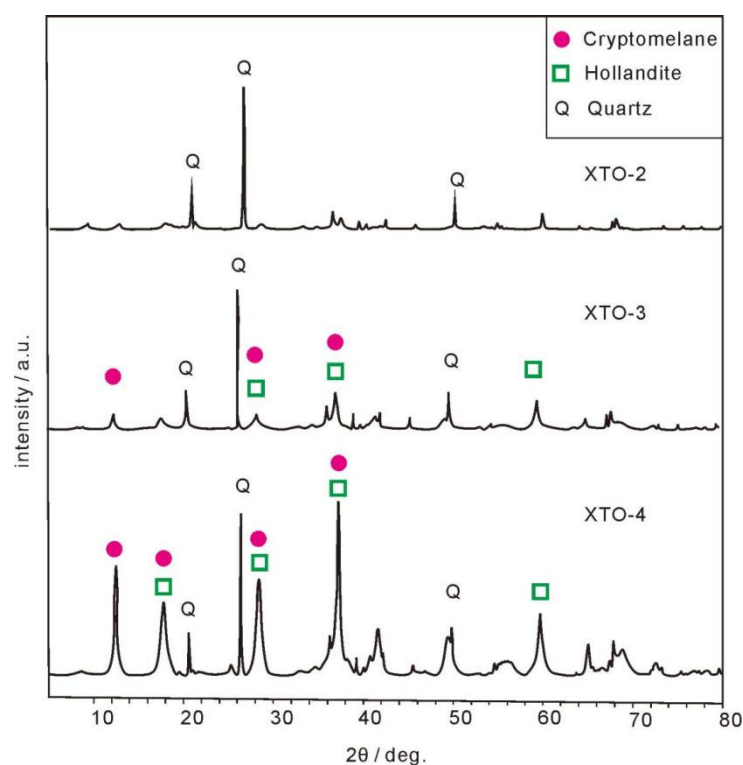


Figure 6. Representative powder diffractograms of the Mn-oxide ore samples from the Xiangtan deposit.

Rietveld refinement was performed on samples of hand-picked Mn-oxide minerals. Results show that the natural cryptomelane is monoclinic crystal system (space group $I2/m$) and its cell parameters were given as $a_0 = 9.93 (\pm 0.06) \text{ \AA}$, $b_0 = 2.87 (\pm 0.02) \text{ \AA}$, $c_0 = 9.70 (\pm 0.06) \text{ \AA}$ and $\beta = 90.3643^\circ$.

4.6. Evaluation of Formaldehyde Removal Activity

The results of the 20 h formaldehyde removal experiments are shown in Figure 7 and Table 3. The curve of the removal rate in different containers is presented in Figure 7a. The sample in container B had the best performance, with a maximum removal rate of 80.74% and an average of 74.02%. Container E followed with a maximum removal rate of 79.58% and an average of 71.40%. The maximum and average removal rates in container D were 70.56% and 63.49%, respectively. The maximum removal rate in container C was 63.71%, with an average value of 49.02%.

The variation curve of CO_2 in five sealed glass containers with different test samples is documented in Figure 7b. It can be seen that under the background value of a CO_2 concentration about 640 ppm, the maximum amount of CO_2 generated by decomposition in container E within 5 h was 580 ppm. Samples in container D and B produced similar maximum amounts of 213 and 202 ppm, respectively. The test sample in container C produced the lowest amount of CO_2 (67 ppm).

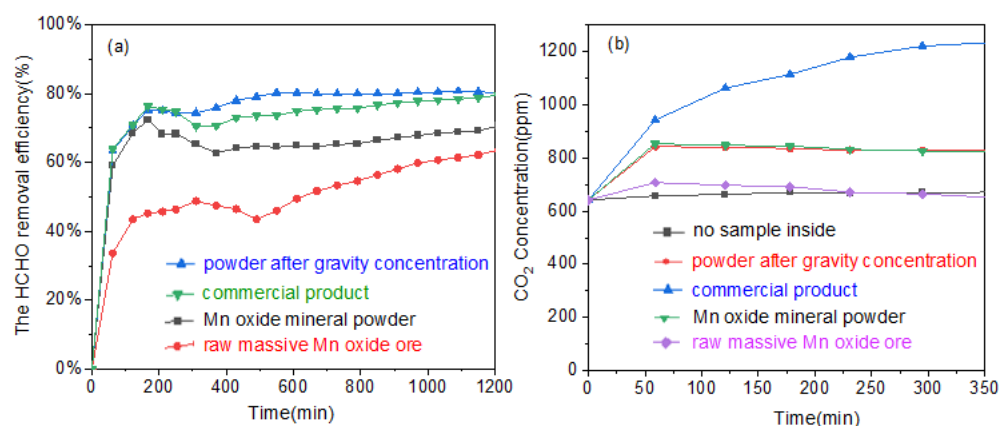


Figure 7. Comparison of formaldehyde catalytic activity of different samples. (a) Comparison of formaldehyde removal efficiency of different samples; (b) comparison of CO₂ concentration of different samples.

Table 3. Experimental results of formaldehyde removal test at room temperature.

The Container Number	Test Samples	Characteristics	The Maximum Formaldehyde Removal Efficiency (%)	The Maximum Amount of CO ₂ (ppm)
A	with no sample inside	/	0	0
B	XTO-3, Mn oxide mineral powder after manual gravity concentration	35 g, 200 mesh	80.74	202
C	XTO-1, the raw massive Mn oxide ore	The volume is approximately equal to 60 cm ³	63.71	67
D	XTO-2, Mn oxide mineral powder	35 g, 200 mesh	70.56	213
E	commercial product	high purity synthetic birnessite loaded on felt, 16 g	79.58	580

5. Discussion

5.1. Characteristics of Main Manganese Oxide Minerals

The supergene manganese oxide minerals are formed by the dissolution, oxidation, migration and precipitation of manganese carbonate or manganese silicate minerals under the influence of atmosphere, water and biology. Acidic water (pH 4.5–5.0) created by the input of organics or bacterial activities near the surface were able to cause Mn²⁺ solutions. Dissolved Mn²⁺ is unstable in high Eh and pH solutions and forms high valence manganese oxide colloids that then move along cracks to percolate slowly through pores in the ores [25]. The chemical composition of weathered solutions may affect the precipitated manganese oxide mineral phases. For example, potassium-rich or aluminum-rich solutions may precipitate cryptomelane or lithiophorite, respectively.

XRD and EPMA results revealed that hollandite supergroup minerals (including cryptomelane and hollandite) predominate among the neo-formed Mn oxide minerals in the Xiangtan deposit and are accompanied by minor pyrolusite, lithiophorite and quartz. Among the Mn oxide minerals mentioned above, pyrolusite has the highest MnO₂ content, averaging up to 99.55%. The content of trace elements in pyrolusite is very low, which is mainly related to the 1 × 1 tunnel crystal structure (Figure 8a). Other trace elements have difficulty entering the crystal structure due to the small diameter of the tunnel [2].

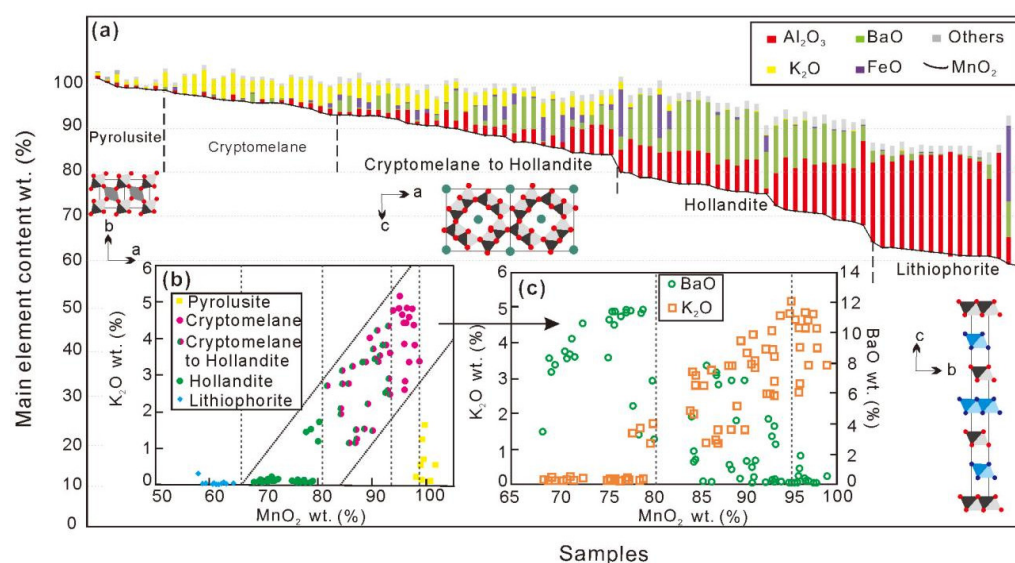


Figure 8. Element composition characteristics (data from EPMA) and corresponding crystal structures of main manganese oxide minerals in Xiangtan manganese deposit. (a) Column chart shows chemical variability of major elements in the identified Mn-oxide phases, and schematic drawing of the crystal structure is presented below correspondingly; red spheres represent O^{2-} , green for tunnel cations, blue for OH^- ; (b) discrimination diagram of Mn oxide phases, according to selected elements (MnO_2 and K_2O); (c) K_2O and BaO content are negatively correlated in cryptomelane and hollandite.

On the basis of the predominant tunnel cation (e.g., hollandite (Ba) and cryptomelane (K)), different minerals in the hollandite supergroup were defined. The crystal structures of cryptomelane and hollandite are almost identical. Thus, both were classified into the octahedral molecular sieve-2 (OMS-2) based on its 2×2 tunnel structure, which is composed of the edge-sharing MnO_6 octahedron with double chains (Figure 8b) [2,26]. Cryptomelane has a higher manganese content (average 93.25%; maximum 99.5%) compared to hollandite (average 78.73%; maximum 93.10%). Natural Mn oxide specimens with end-member compositions are unusual, and EPMA results showed a wide range of K and Ba tunnel cation compositions (Figure 8c). In cryptomelane, K_2O is relatively high, while hollandite is characterized by rich BaO and low K_2O . The content of K_2O in cryptomelane is in the range of 1.25–5.18%. When the K_2O content is lower than 2.5% ($\text{MnO}_2 < 93\%$), it begins to change to hollandite (Figure 8b). At this time, Ba^+ turns out to be the predominant tunnel cation. When the BaO content is higher than 2.92% ($\text{MnO}_2 < 80\%$), the mineral completely changes into hollandite. So cryptomelane and hollandite minerals commonly occur intermixed and graded from one to another. Figure 8c illustrates that K_2O and BaO content are negatively correlated, which reflects their competitive relationship for the location of cations in the center of the tunnel.

Samples of manganese oxide ore from the Xiangtan deposit contain less lithiophorite, which has a low MnO_2 content of 58.87–64.35%. The lithiophorite has a layer structure which consists of a stack of sheets of MnO_6 octahedra alternating with sheets of $\text{Al}(\text{OH})_6$ octahedra (Figure 8a).

5.2. Crystallochemical Characteristics of the Cryptomelane

Cryptomelane, equivalent to $\alpha\text{-MnO}_2$ and first named by Richmond [27], is one of the main constituent minerals of supergenetic manganese oxide. The main characteristics of natural cryptomelane in this area are poor crystallinity, fine grain to the nanometer level and a crystal structure of a low degree of order. Since the monoclinic unit cell of cryptomelane in the Xiangtan manganese deposit has a very short b axis ($2.87 (\pm 0.02) \text{ \AA}$), a fast growth along it can be expected. Natural cryptomelane nanorods exhibit anisotropic

growth behavior, with typical diameters of 20–100 nm and lengths of about 1–20 μm as indicated by detailed SEM and TEM analyses (Figure 5a–d).

The crystallochemical formula of the cryptomelane was calculated as $(\text{K}_{0.36\sim1.48}\text{Ba}_{0\sim1.02}\text{Ca}_{0.01\sim0.05})_{0.44\sim1.79}(\text{Mn}_{6.24\sim7.72}\text{Al}_{0\sim1.45}\text{Fe}_{0\sim1.17}\text{P}_{0\sim0.12}\text{Si}_{0.01\sim0.08})_{7.68\sim8.41}\text{O}_{16}$ (theoretical formula $\text{K}_{0\sim2}\text{Mn}_8\text{O}_{16}$) [28]. The total number of tunnel cations in natural cryptomelane of the Xiangtan Mn deposit is less than 2, and the total number of Mn ions is fewer than 8 (some Mn position sites were accompanied by the substitution of Al, Fe, P and Si ions). Thus, it is clear that cationic defects exist in K and Mn position sites. Wang et al. [29] attempted to alter the electronic structure of catalyst surface sites by adjusting the MnO_x catalyst defects. The results showed that cationic defects have a significant positive effect on the catalytic oxidation activity of formaldehyde [28]. The presence of the tunnel cations also indicated that natural cryptomelane is actually a mixed-valent compound. Mn primarily presents as Mn^{4+} with a small amount of Mn^{3+} or Mn^{2+} ions [30], which is beneficial for strengthening its activity [29,31].

Considerable attention has been paid to the tunnel structure in cryptomelane due to its excellent catalytic performance [32]. As one of the manganese oxide octahedral molecular sieve materials, cryptomelane is often referred to as OMS-2. It has 2×2 and 1×1 tunnel structures and two double edge-sharing MnO_6 octahedral chains corner-connected to form one-dimensional tunnels. The natural cryptomelane of the Xiangtan manganese deposit contains V-sites (vacant sites within the unit cell) and cations (mainly K^+). According to the crystal structure model of cryptomelane, V-sites exist in a 2×2 tunnel, with a cross-section of $d_1 = 0.4667\text{nm}$, $d_2 = 0.4703\text{nm}$ (Figure 9a). Whereas the charge imbalance in a natural cryptomelane framework is supplemented by K^+ and other cations (Ba^{2+} and Ca^{2+}) located in the one-dimensional tunnels, the unit cell containing cations reduces the cross-section by 74% ($d_1 = 0.2392\text{ nm}$, $d_2 = 0.2393\text{ nm}$) and has a smaller aperture compared to synthetic cryptomelane [33]. The presence of tunnel cations could enhance the structural stability of cryptomelane nanofibers [34], and a certain number of V-sites is necessary to relax the electrostatic repulsion between tunnel cations [35,36].

5.3. Catalyst Activity of Formaldehyde by Natural Cryptomelane

Figure 7 shows the catalytic activity of the natural manganese oxides (cryptomelane being the major) and synthetic birnessite products in formaldehyde removal from the air over time. The powder after gravity concentration clearly exhibited the highest catalytic activity among the test samples. This may be due to the higher manganese content of the sample after gravity enrichment and to the larger surface area of the sample after being crushed to about 200 mesh compared with the untreated bulk sample. Under the experimental conditions mentioned above, the removal efficiency of formaldehyde reached maximum value within 200 min of reaction at room temperature (Figure 7a). In Figure 7b, the cumulative CO_2 content generated by formaldehyde oxidation reached maximum value at about 50 min, except for the synthetic birnessite products. It may suggest that the catalytic oxidation of formaldehyde by natural manganese oxide samples mostly occurred within the first 50 min of the reaction and the subsequent reduction in formaldehyde mainly decreased by adsorption.

The catalytic oxidation process of formaldehyde on a metal oxide catalyst follows the Mars-Van Krevelen (MVK) mechanism [37]. Formaldehyde molecules are first adsorbed to the surface of the catalyst, oxidized into the intermediate HCOOH , and then H_2O and CO_2 are product. Section 5.2 mentioned that a certain amount of cationic vacancy exists on the surface of natural cryptomelane, which leads to various types of surface-adsorbed reactive oxygen species. Those reactive oxygen species, which act as active centers of oxidation to convert formaldehyde into CO_2 rapidly [8,33].

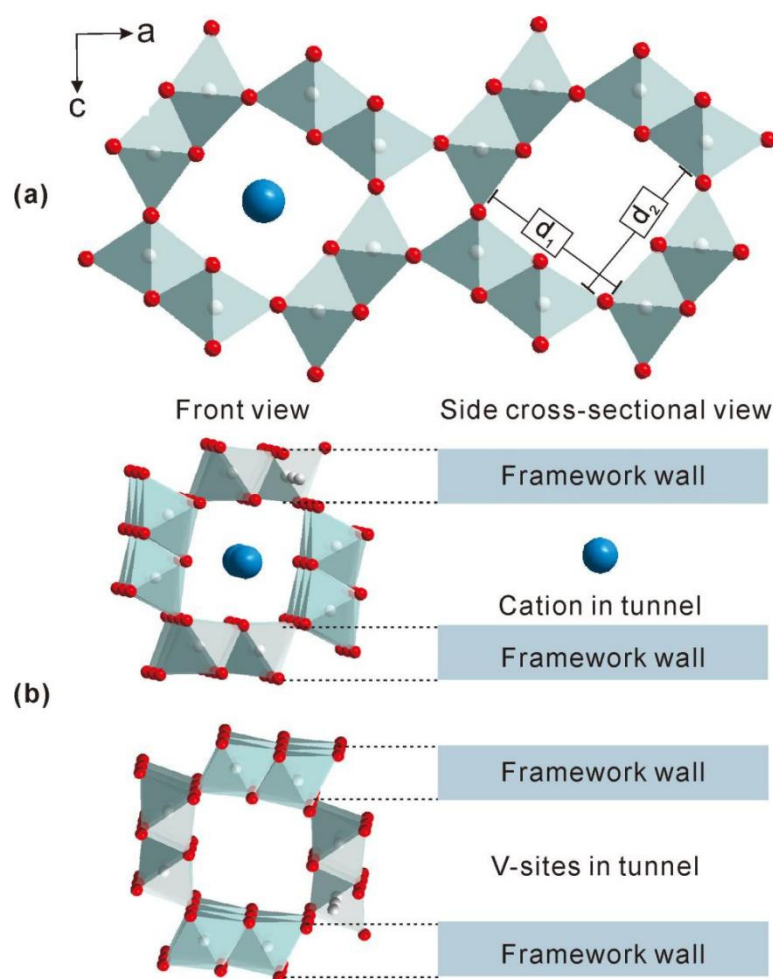


Figure 9. Schematic drawing of the crystal structure of natural cryptomelane. (a) The crystal structure is viewed down the b axis of the monoclinic unit cell. Red, white, and blue balls represent O, Mn, and K, respectively. (b) Perspective view of a single tunnel of natural cryptomelane (front view and side cross-sectional view) showing the cation or V sites inside the tunnel.

As the reaction progresses, the surface reactive oxygen species decrease gradually. Then, the abundance of lattice oxygen in the catalyst is also critical for formaldehyde oxidation [38]. Natural cryptomelane from the Xiangtan deposit has a high MnO₂ content (up to 99.5%), which enhances the lattice oxygen to promote the catalytic oxidation of formaldehyde [10,39,40]. In addition, the presence of an alkali can improve the catalytic activity of the catalyst [41,42]. K⁺ increases the mobility of lattice oxygen by weakening the M–O bond of MnO₂, thus making lattice oxygen more active. Experiments have shown that deep oxidation of formaldehyde into CO₂ occurs even in the absence of molecular O₂ [43]. The K₂O contents of powder after gravity concentration (Table 1) and natural cryptomelane (Table S1) from the Xiangtan deposit show that cryptomelane is the main catalyst for formaldehyde oxidation, which contains a high amount of K₂O (above 3%).

Luo et al. [44] reported that the special 2 × 2 tunnel structure of cryptomelane had higher catalytic activity than the 3 × 3 tunnel structure of todorokite in the complete oxidation of benzene or ethanol in air. Chen et al. [32] prepared three different square-tunnel manganese oxides to test their capacity for formaldehyde catalytic oxidation. The results also suggested that the 2 × 2 tunnel structure of cryptomelane showed much higher catalytic activity than did the 1 × 1 tunnel pyrolusite or 3 × 3 tunnel todorokite. In this study, we explored the formaldehyde sorption and catalyst properties of natural cryptomelane, a molecular sieve of monoclinic crystal system composed of mixed-valent manganese oxide octahedra units. Figure 9 shows the tunnel width for natural cryptomelane, with cations

(0.24 nm) or V-sites (0.47 nm) excluding allowance for van der Waals (vdW) interactions. This tunnel width is the distance between the centers of framework ions and the intra-tunnel cations or oxygen ions of the two MnO_6 octahedra on each side of the 2×2 tunnel. Another case was considered, in which the framework atoms occupied the interspace of the tunnel, with radius equal to the vdW radius of the species. The tunnel width for the unit cell of natural cryptomelane containing V sites was approximately 0.2 nm including the vdW radii (obtained by subtracting the diameter of O^{2-} ions: about 0.28 nm) [45], whereas the unit cell containing cations in the tunnel was impenetrable for other molecules even allowing for vdW interactions at ordinary temperatures. Although the value of 0.2 nm depended on the O^{2-} radius value in the literature, which is small enough, both H_2O and NH_3 with diameters below 0.26 nm could be inserted into the 2×2 tunnel structure with the aid of a strong interaction with the surface of the cryptomelane [46,47]. The dynamic diameter value of formaldehyde is 0.24 nm [32], close to that of effective tunnel diameter of natural cryptomelane of the Xiangtan deposit. Thus, the tunnel size of natural cryptomelane may probably be suitable for the adsorption of formaldehyde molecules, which leads to its high catalytic activity for oxidizing formaldehyde at room temperature.

6. Conclusions

Manganese oxide ores are exceptionally fine-grained and cryptocrystalline, consisting primarily of cryptomelane, along with minor pyrolusite, hollandite, lithiophorite, limonite and quartz. The formula for natural cryptomelane from the Xiangtan manganese deposit is $(\text{K}_{0.36-1.48}\text{Ba}_{0-1.02}\text{Ca}_{0.01-0.05})_{0.44-1.79}(\text{Mn}_{6.24-7.72}\text{Al}_{0-1.45}\text{Fe}_{0-1.17}\text{P}_{0-0.12}\text{Si}_{0.01-0.08})_{7.68-8.41}\text{O}_{16}$. It is a monoclinic $\text{I}2/\text{m}$ space group, with cell dimensions of $a_0 = 9.93 (\pm 0.06) \text{ \AA}$, $b_0 = 2.87 (\pm 0.02) \text{ \AA}$, $c_0 = 9.70 (\pm 0.06) \text{ \AA}$ and $\beta = 90.3643^\circ$.

From the crystal structure modeling of cryptomelane and allowing for vdW interactions, the unit cell containing V-sites in a 2×2 tunnel had a cross-cutting width of $d_1 = 0.4667 \text{ nm}$, $d_2 = 0.4703 \text{ nm}$. Whereas containing cations reduced the cross-cutting area size by 74% to $d_1 = 0.2392 \text{ nm}$, $d_2 = 0.2393 \text{ nm}$.

Mn oxide minerals from the Xiangtan deposit (primarily cryptomelane) are probably effective adsorbents and catalysts for removing formaldehyde in a static environment under room temperature. The removal rate of formaldehyde in this study was as high as 80.74%, and the maximum accumulative release value of CO_2 was 202 ppm during oxidation. Thus, the present study also provided a viable mechanism for determining the origin of catalytic oxidation of formaldehyde by natural Mn oxide ores. The distinct catalytic activity of the Mn oxide minerals from the Xiangtan deposit for oxidizing formaldehyde at room temperature can be attributed to a certain amount of cationic vacancy, the existence of K^+ in the 2×2 tunnel (making lattice oxygen more active), and a suitable tunnel size of natural cryptomelane.

7. Patents

This achievement has been submitted to the State Intellectual Property Office of the People's Republic of China for an invention patent named "A natural mineral material and its application in adsorption and decomposition of formaldehyde and Air purification". The application number is: 22110173928.X.

Supplementary Materials: The following supporting information can be downloaded at: <https://www.mdpi.com/article/10.3390/min12050552/s1>, Table S1: EPMA results of the Mn oxide minerals in the Xiangtan deposit.

Author Contributions: Writing—original draft preparation, L.Z.; writing—review and editing, S.N.; supervision and sample collection, X.N. and F.H.; experimental analysis and investigation, X.N., L.L., T.C., Y.W. and L.M.; graph visualization, H.W. and M.Z. All authors have read and agreed to the published version of the manuscript.

Funding: This study is sponsored by the Science and Technology Innovation Program of China Metallurgical Geology Bureau (grant no. CMGBK202106), “Geology of mineral resources in China” from China Geological Survey (Grant No. DD20221695, DD20190379) and the environmental mineralogy and preliminary application study on manganese oxides from low-grade manganese ores in Hunan and Guangxi.

Data Availability Statement: Some data presented in this study are included within the article. Other data are available on request from the corresponding author Sida Niu.

Acknowledgments: We are grateful to Zhenyu Chen for EPMA analysis. Many thanks are given to Lin Li and Guangyao Liu for their help with the XRD experiments. We thank colleagues from China Metallurgical Geology Bureau of Geological Prospecting Institute of Hunan for their support during the sample collection.

Conflicts of Interest: The authors declare no conflict of interest.

References

1. Turekian, K.K.; Wedepohl, K.L. Distribution of the elements in some major units of the earth’s crust. *Geol. Soc. Am. Bull.* **1961**, *72*, 175–192. [\[CrossRef\]](#)
2. Post, J.E. Manganese oxide minerals: Crystal structures and economic environmental significance. *Proc. Natl. Acad. Sci. USA* **1999**, *96*, 3447–3454. [\[CrossRef\]](#) [\[PubMed\]](#)
3. Prasad, V.S.; Chaudhuri, M. Removal of bacteria turbidity from water by chemically treated manganese iron ores. *Aqua* **1995**, *44*, 80–82.
4. Ghodbane, O.; Pascal, J.L.; Favier, F. Microstructural effects on Charge Storage Properties in MnO₂ based Electrochemical Supercapacitors. *ACS Appl. Mater. Interfaces* **2009**, *1*, 1130. [\[CrossRef\]](#)
5. Huang, M.; Li, F.; Dong, F.; Zhang, Y.; Zhang, L.-L. MnO₂-based nanostructures for high-performance supercapacitors. *J. Mater. Chem. A* **2015**, *3*, 21380–21423. [\[CrossRef\]](#)
6. Huang, H.; Xu, Y.; Feng, Q.; Leung, D.Y.C. Low temperature catalytic oxidation of volatile organic compounds: A review. *Catal. Sci. Technol.* **2015**, *5*, 2649–2669. [\[CrossRef\]](#)
7. Nie, L.; Yu, J.; Jaroniec, M.; Tao, F.-F. Room-temperature catalytic oxidation of formaldehyde on catalysts. *Catal. Sci. Technol.* **2016**, *6*, 3649–3669. [\[CrossRef\]](#)
8. Su, J.; Chen, C.; Guo, Y.; Xu, H.; Ke, Q. OMS-2-based catalysts with controllable hierarchical morphologies for highly efficient catalytic oxidation of formaldehyde. *J. Hazard. Mater.* **2019**, *380*, 120890. [\[CrossRef\]](#)
9. Sekine, Y.; Nishimura, A. Removal of formaldehyde from indoor air by passive type air-cleaning materials. *Atmos. Environ.* **2001**, *35*, 2001–2007. [\[CrossRef\]](#)
10. Tang, X.-F.; Li, Y.-G.; Huang, X.-M.; Xu, Y.-D.; Zhu, H.-Q.; Wang, J.-G.; Shen, W.-J. MnO_x-CeO₂ mixed oxide catalysts for complete oxidation of formaldehyde: Effect of preparation method/calcination temperature. *Appl. Catal. B Environ.* **2006**, *62*, 265–273. [\[CrossRef\]](#)
11. Tang, X.-F.; Chen, J.-L.; Huang, X.-M.; Xu, Y.-D.; Shen, W.-J. Pt/MnO_x-CeO₂ catalysts for the complete oxidation of formaldehyde at ambient temperature. *Appl. Catal. B Environ.* **2008**, *81*, 115–121. [\[CrossRef\]](#)
12. Adelodun, A.A. Influence of Operation Conditions on the Performance of Non-thermal Plasma Technology for VOC Pollution Control. *J. Ind. Eng. Chem.* **2020**, *92*, 41–55. [\[CrossRef\]](#)
13. Brown, G.E.; Calas, G. Mineral-aqueous solution interfaces and their impact on the environment. *Geochem. Perspect.* **2012**, *1*, 483–742. [\[CrossRef\]](#)
14. Lu, A.H.; Li, Y.; Liu, F.-F.; Liu, Y.-W.; Ye, H.; Zhuang, Z.-Y.; Li, Y.-Z.; Ding, H.-R.; Wang, C.-Q. The photogeochemical cycle of Mn oxides on Earth’s surface. *Mineral. Mag.* **2021**, *85*, 22–38. [\[CrossRef\]](#)
15. Wang, J.; Zhang, P.; Li, J.; Jiang, C.; Yunus, R.; Kim, J. Room-temperature oxidation of formaldehyde by layered manganese oxide: Effect of water. *Environ. Sci. Technol.* **2015**, *49*, 12372–12379. [\[CrossRef\]](#)
16. Li, J.-G.; Zhang, P.-Y.; Wang, J.-L.; Wang, M.-X. Birnessite-type manganese oxide on granular activated carbon for formaldehyde removal at room temperature. *J. Phys. Chem. C* **2016**, *120*, 24121–24129. [\[CrossRef\]](#)
17. Birkner, N.; Navrotsky, A. Thermodynamics of manganese oxides: Sodium, potassium, and calcium birnessite and cryptomelane. *Proc. Natl. Acad. Sci. USA* **2017**, *114*, E1046–E1053. [\[CrossRef\]](#)
18. Potter, R.M.; Rossman, G.R. The tetravalent manganese oxides; identification, hydration, structural relationships by infrared spectroscopy. *Am. Mineral.* **1979**, *64*, 1199–1218.
19. *Mineral Commodity Summaries 2019*; U.S. Geological Survey: Reston, VA, USA, 2019; 204p. [\[CrossRef\]](#)
20. Gao, X.; Lu, A.-H.; Qin, S.; Zheng, Z. The refinement of crystal unit cell parameters of native cryptomelane in the supergene oxidation zone of the Xiangtan manganese deposit, Hunan Province. *Acta Petrol. Mineral.* **2003**, *1*, 77–79. (In Chinese)
21. Gao, X.; Lu, A.-H.; Zheng, Z.; Jia, X.-X. Natural oxide octahedral molecular sieve OMS-2—The study of the characters of microstructure by for HRTEM cryptomelane of Xiangtan manganese deposit, Hunan province. *J. Mineral. Petrol.* **2005**, *3*, 52–57. (In Chinese)

22. Zheng, J.-Y.; Zhao, W.-K.; Wang, X.; Zheng, Z.; Han, C.-B. Electric-enhanced hydrothermal synthesis of manganese dioxide for the synergistic catalytic of indoor low-concentration formaldehyde at room temperature. *Chem. Eng. J.* **2020**, *401*, 125790. [[CrossRef](#)]
23. Liu, X.-F.; Wang, Q.-S.; Gao, X.-J. *Manganese Deposits of Guizhou, China*; Guizhou People Press: Guiyang, China, 1989; pp. 1–194. (In Chinese)
24. Fan, D.; Yang, P. Introduction to classification of manganese deposits of China. *Ore Geol. Rev.* **1999**, *15*, 1–13. [[CrossRef](#)]
25. Pracejus, B.; Bolton, B.R.; Frakes, L.A. Nature and development of supergene manganese deposits, Groote Eylandt, Northern Territory, Australia. *Ore Geol. Rev.* **1988**, *4*, 71–98. [[CrossRef](#)]
26. Lu, A.-H.; Gao, X.; Qin, S.; Wang, C.-Q. Cryptomelane $K_xMn_{8-x}O_{16}$: Natural active octahedral molecular sieve OMS-2. *Chin. Sci. Bull.* **2003**, *48*, 920–923. [[CrossRef](#)]
27. Richmond, W.E.; Fleischer, M. Cryptomelane, a new name for the commonest of the “psilomelane” minerals. *Am. Miner.* **1942**, *27*, 607–610.
28. Sato, H.; Enoki, T.; Yamaura, J.I.; Yamamoto, N. Charge localization and successive magnetic phase transitions of mixed-valence manganese oxides $K-1.5(H_3O) \times Mn_8O_{16}$ ($0 < x < 0.5$). *Phys. Rev. B* **1999**, *59*, 12836–12841.
29. Wang, J.-L.; Jiang, C.-J.; Zhou, P.; Zhang, P.-Y.; Yu, J.-G. The effect of manganese vacancy in birnessite-type MnO_2 on room-temperature oxidation of formaldehyde in air. *Appl. Catal. B Environ.* **2017**, *204*, 147–155. [[CrossRef](#)]
30. Post, J.E.; Dreele, R.B.V.; Buseck, P.R. Symmetry displacement in hollandites: Structure refinements of hollandite, cryptomelane priderite. *Acta Crystallogr.* **1982**, *38*, 1056–1065. [[CrossRef](#)]
31. Qi, Q.-P.; Zhang, W.-R.; Zhang, Y.-S.; Bai, G.-M.; Wang, S.-W.; Peng, L. Formaldehyde oxidation at room temperature over layered MnO_2 . *Catal. Commun.* **2021**, *153*, 106293. [[CrossRef](#)]
32. Chen, T.; Dou, H.-Y.; Li, X.-L.; Tang, X.-F.; Li, L.-H.; Hao, J.-M. Tunnel structure effect of manganese oxides in complete oxidation of formaldehyde. *Microporous Mesoporous Mater.* **2009**, *122*, 270–274. [[CrossRef](#)]
33. Espinal, L.; Wong-Ng, W.; Kaduk, J.A.; Allen, A.J.; Suib, S.L. Time-Dependent CO_2 Sorption Hysteresis in a One-Dimensional Microporous Octahedral Molecular Sieve. *J. Am. Chem. Soc.* **2012**, *134*, 7944–7951. [[CrossRef](#)] [[PubMed](#)]
34. Gao, T.; Norby, P. Frame stability of tunnel-structured cryptomelane nanofibers: The role of tunnel cations. *Eur. J. Inorg. Chem.* **2013**, *28*, 4948–4957. [[CrossRef](#)]
35. De Guzman, R.N.; Shen, Y.F.; Neth, E.J.; Suib, S.L.; O’Young, C.L.; Levine, S.; Newsam, J.M. Synthesis characterization of octahedral molecular sieves OMS-2 having the hollandite structure. *Chem. Mater.* **1994**, *6*, 815–821. [[CrossRef](#)]
36. Vasconcelos, P.M.; Wenk, H.R.; Echer, C. In-situ study of the thermal behavior of cryptomelane by high-voltage analytical electron microscopy. *Am. Mineral.* **1994**, *79*, 80–90.
37. Sekine, Y. Oxidative decomposition of formaldehyde by metal oxides at room temperature. *Atmos. Environ.* **2002**, *36*, 5543–5547. [[CrossRef](#)]
38. Zhang, J.-H.; Li, Y.-B.; Wang, L.; Zhang, C.-B.; He, H. Catalytic oxidation of formaldehyde over manganese oxides with different crystal structures. *Catal. Sci. Technol.* **2015**, *5*, 2305–2313. [[CrossRef](#)]
39. Wu, Y.; Lu, Y.; Song, C.-J.; Ma, Z.-C.; Xing, S.-T.; Gao, Y.-Z. A novel redox-precipitation method for the preparation of α - MnO_2 with a high surface Mn^{4+} concentration and its activity toward complete catalytic oxidation of o-xylene. *Catal. Today* **2013**, *201*, 32–39. [[CrossRef](#)]
40. Li, K.; Chen, C.; Zhang, H.-B.; Hu, X.-J.; Sun, T.-H.; Jia, J.-P. Effects of phase structure of MnO_2 morphology of δ - MnO_2 on toluene catalytic oxidation. *Appl. Surf. Sci.* **2019**, *496*, 143662. [[CrossRef](#)]
41. Hou, J.-T.; Liu, L.-L.; Li, Y.-Z.; Mao, M.-Y.; Lv, H.-Q.; Zhao, X.-J. Tuning the K^+ concentration in the tunnel of OMS-2 nanorods leads to a significant enhancement of the catalytic activity for benzene oxidation. *Environ. Sci. Technol.* **2013**, *47*, 13730–13736. [[CrossRef](#)]
42. Xu, F.; Huang, Z.-W.; Hu, P.-P.; Chen, Y.-X.; Zheng, L.; Gao, J.-Y.; Tang, X.-F. The promotion effect of isolated potassium atoms with hybridized orbitals in catalytic oxidation. *Chem. Commun.* **2015**, *51*, 9888–9891. [[CrossRef](#)]
43. Yusuf, A.; Sun, Y.; Snape, C.; He, J.; Wang, C.; Ren, Y.; Jia, H. Low-temperature formaldehyde oxidation over manganese oxide catalysts: Potassium mediated lattice oxygen mobility. *Mol. Catal.* **2020**, *497*, 111204. [[CrossRef](#)]
44. Luo, J.; Zhang, Q.-H.; Huang, A.-M.; Suib, S.L. Total oxidation of volatile organic compounds with hydrophobic cryptomelane-type octahedral molecular sieves. *Microporous Mesoporous Mater.* **2000**, *35–36*, 209–217. [[CrossRef](#)]
45. Bondi, A. van der Waals Volumes Radii. *J. Phys. Chem.* **1964**, *68*, 441–451. [[CrossRef](#)]
46. Wang, Z.-M.; Tezuka, S.; Kanoh, H. Characterization of the structural surface properties of a synthesized hydrous hollandite by gaseous molecular adsorption. *Chem. Mater.* **2001**, *13*, 530–537. [[CrossRef](#)]
47. Kijima, N.; Ikeda, T.; Oikawa, K.; Izumi, F.; Yoshimura, Y. Crystal structure of an open-tunnel oxide α - MnO_2 analyzed by rietveld refinements MEM-based pattern fitting. *J. Solid State Chem.* **2004**, *177*, 1258–1267. [[CrossRef](#)]